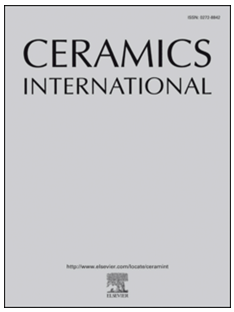

Effect of Fe^{3+} ion doping on photocatalytic ability of nanozirconia ceramic to degrade 2, 4, 6- trichlorophenol

Milica V. Carević, Tatjana D. Savić, Nadica D. Abazović, Miloš D. Mojović, Tatjana B. Novaković, Mirjana I. Čomor

PII: S0272-8842(19)33367-X

DOI: https://doi.org/10.1016/j.ceramint.2019.11.175

Reference: CERI 23544

To appear in: *Ceramics International*

Received Date: 2 August 2019

Revised Date: 11 November 2019

Accepted Date: 20 November 2019

Please cite this article as: M.V. Carević, T.D. Savić, N.D. Abazović, Miloš.D. Mojović, T.B. Novaković, M.I. Čomor, Effect of Fe^{3+} ion doping on photocatalytic ability of nanozirconia ceramic to degrade 2, 4, 6- trichlorophenol, *Ceramics International* (2019), doi: https://doi.org/10.1016/j.ceramint.2019.11.175.

Effect of Fe^{3+} ion doping on photocatalytic ability of nanozirconia ceramic to degrade 2, 4, 6- trichlorophenol

Milica V. Carević[1], Tatjana D. Savić[1], Nadica D. Abazović[1], Miloš D. Mojović[2], Tatjana B. Novaković[3], Mirjana I. Čomor*[1]

[1]Vinča Institute of Nuclear Sciences, University of Belgrade, P.O. Box 522, 11001 Belgrade, Serbia

[2]Faculty of Physical Chemistry, University of Belgrade, Studentski Trg 1, 11000 Belgrade, Serbia

[3]IChTM- Department of Catalysis and Chemical Engineering, University of Belgrade, Njegoševa 12, 11000 Belgrade, Serbia

*Correspondence should be addressed to Mirjana I. Čomor, E-mail: mirjanac@vin.bg.ac.rs; mirjanacom@gmail.com

Abstract

Pure and a series of Fe^{3+} doped zirconia nanopowders were synthesized combining colloidal chemistry and solvothermal method from organometallic precursors in order to correlate doping and properties of zirconia matrix. After annealing of washed nanopowders at 600°C, detailed characterization was performed using X-ray diffraction, UV/vis absorption and luminescence, infrared and electron paramagnetic spectroscopy, transmission electron microscopy and BET measurements. Zirconia samples had mixed monoclinic and tetragonal crystalline phase; increasing Fe^{3+} ions concentration was followed by increasing of tetragonal phase share. In the sample with highest Fe^{3+} concentration, hematite can be detected. Also, UV/Vis spectrophotometry showed that Fe^{3+} doping lowers effective band gap of zirconia matrix from 4.5 eV (bulk value) to 2.1 eV for doped/nanocomposite samples. EPR measurements proved presence of dopant and showed that isolated Fe^{3+} ions in zirconia matrix exist in both crystalline phases; monoclinic and tetragonal ($g \sim 4.8$ and $g \sim 4.27$ - 4.2, respectively) surroundings. Zirconia samples were also successfully used as photocatalysts for photocatalytic degradation of 2, 4, 6, trichlorophenol.

Keywords: A. Powders: chemical preparation; B. Electron microscopy; D. ZrO_2; E. Functional application.

1. Introduction

Transition metal oxide ceramic materials, specifically ZrO_2, have wide applications~~, for example~~ such as: catalyst and catalyst support [1], sorbent [2], oxygen sensor [3] and in solid oxide fuel cells [4]. Zirconia band gap energy (E_g), values that can be found in literature, are in the range between 3.25 and 5.1 eV [5, 6]. As stated in

literature, differences can be caused by the preparation technique of zirconia and the presence of dopants/defects in the matrix. The most customary used value is approximately 5.0 eV; with a conduction band potential of −1.0V and the valence band potential of +4.0V vs. NHE at pH 0 [7]. The high band gap energy, stability, and the high negativity of the conduction band edge potential granted its potential use as a photocatalyst in advance oxidation processes (AOPs). In AOPs, potent reactive species, radicals, are formed by consecutive chemical reactions in aqueous solutions [8]. Among AOPs, heterogeneous photocatalysis have an important role due to its efficacy in degradation of several groups of organic pollutants which withstand degradation in any other way, for example: phenolic compounds, pesticides and pharmaceuticals [9]. Despite the fact that the absorption maximum of chemically pure ZrO_2 ~~has absorption maximum~~ is around 250 nm, some synthesized probes have an observable optical activity in the near UV and visible range of the Solar spectrum, induced by the presence of well-known color centers/defects in the zirconia matrix [10]. Literature data shows that ~~recently~~, zirconia nanostructures were recently tested as photocatalysts for degradation of dyes [6, 7, 11], phenol-like compounds [12-17]; while light applied for activation of the photocatalyst had energies significantly below the expected intrinsic absorption threshold/band gap energy of zirconia. The reasons for that are most ~~probably~~ likely the presence of various impurity levels and intra-band states assigned to defects, which are responsible for its photoactivity [7, 10, 13-17]. Improving of photocatalytic applicability of zirconia is a research topic in many laboratories ~~all over~~ across the world; the most common methods are: metal [13,17-23] or nonmetal doping [24, 25], coupling with semiconductors with suitable/ narrower band gap energy [15, 26] or with conductive polymers [16] or graphene-based composite [27] that may cause

the increase~~ing~~ of the visible light sensitivity and/or control over the electron–hole recombination process. Transitional metal-doping of zirconia matrix can influence the adsorption ability on the semiconductor NPs surface of different organic/inorganic pollutants. Adsorption is one of the major steps in heterogeneous photocatalysis, so efficacy of photodegradation of pollutants can be affected in this way. Other factors that can affect photocatalytic activity of ZrO_2 are: crystalline phase purity, nanoparticle sizes, inherent properties of dopant ions, and applied method of synthesis/modification [6, 20, 28, 29]. Lopez et al. [17], ~~presented~~ in their study of photocatalytic activity of ZrO_2 particles doped with transition metal ions such as Mn^{2+}, presented the beneficial influence of doping – doping of zirconia with Ce^{4+} ions induced intra-band gap states, ~~that process~~which resulted in improving its visible light activity [18]. One of the most suitable dopants for ZrO_2 can be Fe^{3+} ions because of the smaller ion radius (0.64 Å) compared to Zr^{4+} (0.80 Å) [21, 22] and its ability to increase number of oxygen vacancies in the zirconia matrix [22]. A lot of different methods were used for synthesis of Fe^{3+} doped ZrO_2; the most usual being sol-gel [20-22], mechanochemical/ ball milling [23]. Literature results are mostly positive, devoted to the improvement of photocatalytic activity of doped zirconia compared to pure material, when UV or visible light was used. The common fact is limiting quantity of Fe^{3+} ions that can be incorporated in zirconia matrix, before development of iron oxide as a crystallographic phase and formation of nanocomposite.

In this study, we systematically doped zirconia matrix with Fe^{3+} ions, with nominal concentrations: 1, 5, 10 and 20 atomic % (a.%). We used the solvothermal method as one of the most reproducible and controllable one. The aim was to see if the presence of iron ions can influence the properties of the matrix and in which way. Used

concentrations of dopant are relatively high, but we considered limitations of incorporation of Fe^{3+} ions in zirconia samples without formation of iron oxide or mixed oxide phase [22]. The presence of iron oxide phase can have a positive effect on photocatalytic proces [30] due to the positions of band edges and extent of band gaps of oxides. This can be considered as continuation of our experiments in which we probed ZrO_2 as the photocatalyst for degradation of model pollutants using artificial Solar light [13, 15, 16].

2. Material and methods

2.1. Materials

All chemicals were of analytical grade (highest available) and were used without further purification. The following commercial chemicals were used: Zirconium (IV) propoxide (ZIP, Sigma-Aldrich, 70 wt % solution in 1-propanol), Iron (III) acetylacetonate (Aldrich, 99.9+%); 2, 4, 6-trichlorophenol (TCP, Alpha Aesar, 98 %), nitric acid (J.T. Baker, 65 %), isopropanol (J.T. Baker, >99.8 %), methanol (J.T. Baker, HPLC grade), tert-Butyl alcohol (TB, Fluka, p.a., ≥99.5%) and p-Benzoquinone (BQ, Sigma-Aldrich, reagent grade, ≥98%). ~~In all experiments d~~Deionized water from Mili Q system was used (resistivity ≥ 18.2 MΩ cm^{-1}) in all experiments.

2.2. Sample preparation

Pure and doped zirconium oxide nanopowders were synthesized by solvothermal treatment. In a Teflon vessel (23 mL volume) 5 mL of water and 4 mL of isopropanol were mixed at ~ 0 °C. The pH was adjusted to ~2, by using nitric acid. Then, appropriate amounts of Iron (III) acetylacetonate (0, 0.0045, 0.0225, 0.045 and 0.09 g for pure zirconia and zirconia doped with 1, 5, 10, 20 % Fe ions) were added. Mixture

was stirred for 15 min at 0 ºC. Then 0.57 mL of ZIP was added dropwise, mixture was stirred vigorously in ice bath. After 15 min of stirring, dispersion was autoclaved 24 h at 150 °C. The obtained powders were washed using water until the water reached pH = 6. Finally, the powder was separated from the washing solution by centrifugation, dried at 100 °C until constant weight and annealed at 600° C for 3 hours. The quantitative chemical analysis of the obtained nanomaterials was realized by inductively coupled plasma optical emission spectroscopy (ICP–OES) (Spectroflame ICP, 2.5 kW, 27 MHz). The measurements were performed by measuring the intensity of the radiation emitted by each element (Zr and Fe) at specific wavelength. Obtained results revealed that actual percentages of Fe^{3+} ions incorporated in ZrO_2 structures were 0.6 a.% for 1-ZrO_2, 3.6 a.% for 5-ZrO_2, 7.6 a.% for 10 – ZrO_2 and ~ 10 a.% for 20- ZrO_2. Real concentrations of incorporated iron ions were approximately 30% lower than nominal, except for 20 – ZrO_2 where no more than 10 a.% was incorporated in ZrO_2 matrix, most probably due to saturation. Nevertheless, samples were denoted in simplified way, according stoichiometric quantities of Fe ions, as ZrO_2, 1-ZrO_2, 5-ZrO_2, 10-ZrO_2 and 20-ZrO_2.

2.3. Sample characterization; 2.4. Photodegradation procedure; 2.5. Analytical procedure

All details regarding XRD, ICP-OES, TEM, UV/Vis absorption and luminescence spectroscopy, EPR and BET measurements can be found in Supplemental materials (SM) as well as photocatalytic degradation of TCP procedure and subsequent analytical procedures (HPLC and TOC techniques), because of similarities with already published papers by Carević et.al. [13-16]. In order to make following R&D section clear without

reading SM, here are the details regarding photocatalytical experiments: photocatalysis was carried out at atmospheric pressure and room temperature (20°C); 20 mg of catalyst was dispersed in 40 mL (0.5 mg/mL) of TCP aqueous solution, 5 x 10^{-4} mol/L; dispersions were illuminated using Vitalux lamp that simulates Solar spectrum at natural pH (~ 7).

3. Results and discussion

3.1. Crystallinity, morphology and textural properties of zirconia-based NP

XRD patterns of all synthesized nanostructured samples are presented in Figure 1. Pure zirconia sample contains the bland of monoclinic and tetragonal phases, the influence of annealing process on development of crystallinity, can be seen in Fig. S1 in SM.

The peaks are assigned to tetragonal (t) and monoclinic (m) phase according to JCPDS 81-1544 and Baddeleyite-JCPDS 65-1025 data, respectively. The volume ratio of monoclinic (μ_M) and tetragonal (μ_T) phases in samples were calculated using equations (2) and (3) [29], from the intensity (I)/area of the most prominent peaks: (-111) and (111) for monoclinic and (101) for tetragonal phase:

$$\mu_T = \frac{I_{T(101)}}{I_{M(-111)} + I_{T(101)} + I_{M(111)}} \quad (2)$$

$$\mu_M = 1 - \mu_T \quad (3)$$

Figure 1.

Table 1. The volume share (in percentage) of tetragonal and monoclinic crystalline phases in zirconia samples, calculated using equation (2) and crystalline domains of zirconia powders calculated from XRD data.

Sample	μ_T		μ_M		Tetragonal Crystallite size (nm)	Monoclinic crystallite size (111) (nm)
	Area (%)	Intensity (%)	Area (%)	Intensity (%)		
ZrO_2	47.9	45.05	52.1	54.95	8.3	4.9
1- ZrO_2	41.5	38.5	58.5	61.5	12.3	13.7
5- ZrO_2	60.7	58	39.3	42	12.1	12.6
10- ZrO_2	76.8	79.2	23.2	20.8	9.5	6.8
20- ZrO_2	96.8	95.9	3.2	4.1	9.9	12.3

Table 1 presents summarized data from XRD measurements. Pure zirconia NPs had about 1:1 ratio of tetragonal and monoclinic phase; incorporation of the smallest quantity of Fe^{3+} ions decreased the tetragonal fraction slightly (for about 10 %), for 5-ZrO_2 sample tetragonal fraction started to increase and follow the increase of quantity of Fe^{3+} ions, until the 20-ZrO_2 which had 95% of tetragonal phase and visible hematite crystal phase (marked with star in Fig. 1, 20-ZrO_2). The development of the tetragonal phase in the presence of larger quantities of iron ions could be a consequence of a decrease in the surface free energy in ZrO_2 or of the formation of anionic/oxygen vacancies. The explanation of this effect is based on the large destruction of the surrounding next- nearest neighbors network induced by the presence of Fe^{3+} ions that compete with Zr^{4+} ions for the oxygen vacancies [22] and seems to be dependent to the intrinsic properties of the zirconia matrix. Crystallization in pure ZrO_2, as stated in the literature, the process leading to the monoclinic phase, is initiated at about 350 °C, so the mixture of tetragonal and monoclinic phase can be assigned to impurities or the

nature of the precursor (Zr (IV) propoxide –ZIP). Our data showed that ZrO_2 had a mixture of monoclinic and tetragonal phases, which indicated that some additional process interfered in the transformation of the metastable tetragonal phase into monoclinic. The 600°C as annealing temperature was enough for the development of pure monoclinic phase when $ZrOCl_2$ was used as precursor, as presented by Carević et al, [13]. Obviously, propoxide can form a crystallization matrix, with analogy to Ti-alkoxides [31], which can delay the transformation of m-tetragonal to monoclinic phase. Binary oxide phases, like $ZrFe_2O_5$, could not be found/proved by XRD technique in the doped samples, but hematite was detected in 20-ZrO_2 (Fig. 1). It should be stressed that it is not easy to prove the presence of crystalline zirconium ferrite in zirconia matrix using XRD, due to the similarities of their XRD patterns [32].

Figure 2.

Typical TEM images of zirconia nanoparticles are presented in Fig. 2. All samples, regardless doping, had more or less pronounced spherical shape. Also, sizes are comparable, diameters of about 10 ± 2 nm, similar to sizes calculated from XRD spectra presented in Table 1. For some samples crystalline planes are visible, Fig. 2e, due to excellent crystallization of zirconia. In doped samples a fraction of very small particles can be seen, most probably iron oxide or zirconium ferrite phase, even for small doping levels which cannot be detected using XRD technique.

Textural properties of zirconia-based NPs are presented in Table 2 and Figs. S2 and S3 in SM. All samples are characterized by isotherm type IVa. This type of isotherm can be assigned to adsorption on the material with low porosity or~~, as most probably~~more likely in this case, on the material with predominately mesoporous pore

diameters (2-50 nm). The mesoporosity, by definition, can be described by the characteristic shape of the isotherm curve induced by capillary condensation step, in the range of 0.5-0.8 of relative pressures. The sharp increase of the V_{ads} in the isotherms (Fig. S3), indicated the occurrence of capillary condensation in a narrow-size range of mesopores. Isotherms of all samples are dominated by a H2 type hysteresis loop, suggesting broad distribution of pore structures in this material, with a tendency of making up interconnected webs of pores of different size and shape.

Table 2 Textural properties of zirconia samples.

Sample	S_{BET}, m^2g^{-1}	$V_{p\ 0.98}$,cm^3g^{-1}	D_{max},nm
ZrO_2	53	0.114	8
1- ZrO_2	65	0.166	8
5- ZrO_2	64	0.132	7
10- ZrO_2	80	0.178	6.7
20- ZrO_2	73	0.167	6.4

Addition of Fe^{3+} ions in zirconia matrix induced changes in the textural properties of samples. Depending on the amount of added Fe^{3+} ions, isotherms move along the y-axis and the x-axis, indicating a change in pore volume, shape and distribution of pores of their size (Table 3). BET measurements showed that doping stabilized presence of isolated particles; specific surface area increased with doping. The largest specific surface has 10-ZrO_2 and the smallest pure ZrO_2; the other three samples had specific surfaces between these values: 1-ZrO_2 and 5-ZrO_2 have almost the same S_{BET}, but lower than the S_{BET} of 20- ZrO_2.

3.2. Optical and EPR properties of zirconia samples

In Fig. 3 UV/Vis DR (a) and absorption (b) spectra are presented. Pure ZrO_2 has a sharp decrease of reflection below λ = 400 nm, although tailing in the visible part of the spectra can also be seen. This tailing can be assigned to oxygen vacancies [5]. Perevalov et al. [33] calculated the position of the defect band that can be assigned to oxygen vacancies, to be at 2.2 eV above valence band of zirconia, with a variable width depending on the concentration of defects. In Fig. 3b, an increase of absorption intensity and shift of the absorption threshold to lower energies, with the increasing amount of Fe^{3+} dopant (from 1-20 atomic %). Also, the color of the powders, composite samples, changed from white (pure ZrO_2) to pale pink and finally to orange (20-ZrO_2). The Fe^{3+} doping of the ZrO_2 matrix induced a lowering of the effective band gap; samples with the higher concentrations of added Fe^{3+} ions in the matrix have the greater intensities of absorption in the visible light range ($\lambda \geq 400$ nm). This is, most probably, the result of the shift of the VB edge to less positive values or the shift of the CB edge to more positive values in zirconia or combined regarding the Fe^{3+} content.

Figure 3.

All samples had broad absorption at about 320 nm that can be ascribed to charge transfer from oxygen vacancies to CB of ZrO_2; additionally, Fe^{3+} doped zirconia samples (Fig. 3b curve 10- ZrO_2) had broad absorption band positioned from about 500 to 600 nm which is result of d−d transition of Fe^{3+} ($^2T_{2g} \rightarrow {}^2A_{2g}$, $^2T_{1g}$) or to the interacting, closely situated Fe^{3+} ions (true charge transfer process) via conduction band, id est.: $Fe^{3+} + Fe^{3+} \rightarrow Fe^{4+} + Fe^{2+}$. If the latter statement is true, Fe^{3+} doping of ZrO_2 ~~by~~ with the synthesis procedure described in this study can produce different valences of iron ions (Fe^{4+} and Fe^{2+}) that are distributed through the band gap of ZrO_2, similar to Fe^{3+} doped TiO_2 [31]. ~~As a consequence~~Consequently, the wavelength range of light

that can be absorbed by photocatalyst is widened, ~~enhancing that way~~thus enhancing the nanocomposite's visible-light photocatalytic activity. The Tauc's plots $((\alpha h\upsilon)^2$ versus photon energy, the hυ (eV)) of the nanocomposite powders are shown in the Fig. 4. The apparent band gap energies were obtained by extrapolating the linear portion of the lines to the intersection with the hυ axis (x-axis), at E_g. The apparent band gap energies were in the range from 4.5 eV for pure zirconia to 2.1 eV for the highest doping concentrations (10 and 20 a. %). In the absorption F_{FK} plots (Figs. 3b and 4), the lower energy part compared to the straight part of the spectra which is extrapolated to intersect the hυ axis (x-axis) at E_g, is known as absorption tail or Urbach tail. The energy associated with these transitions is known as Urbach energy and can be calculated from:

$$\alpha = \alpha_o \exp(h\upsilon/E_u) \qquad (4)$$

In the equation (4), α is the absorption coefficient, hυ is photon energy, and E_u is the Urbach energy [31]. Urbach energies are calculated by using plotting of ln α versus (hυ) as shown in Fig. S4, in SM; the reciprocal value of the slope of the linear portion gives the value of E_u. In Table 3, the Urbach energies are listed: the highest value is obtained for pure zirconia due to defects, for doped samples the highest value is for the lowest Fe^{3+} concentration in the ZrO_2 matrix and then decreases with the increase in Fe^{3+} concentration; this can be used as a proof for a hypothesis that energies of defect levels are formed in the band gap of the ZrO_2 (between VB and CB band edges) inducing the narrowing of the intrinsic band gap [31]. As Fe^{3+} ions doping concentration increases, new phase- hematite is slowly formed and ZrO_2 phase is clearing itself from dopant ions and defects, and changes in the absorption spectra can be assigned to the formation of iron oxide phase. For the higher doping concentrations (10 and 20 %) hematite phase

can be responsible for band gap narrowing/ reduction, the value of 2.2 eV resembles the band gap of hematite [30].

Figure 4.

Table 3 Band gap and Urbach energies of pure and doped ZrO_2 samples.

Sample	E_g (eV)	E_u (meV)
ZrO_2	4.5	~ 1500
1-ZrO_2	2.7	434
5-ZrO_2	2.7	265
10-ZrO_2	2.1	223
20-ZrO_2	2.1	220

Table 3 Band gaps calculated from Tauc's plots (Fig. 4) and Urbach energies calculated from absorption spectra presented in Fig. 2b, of zirconia samples. Urbach plots are given in Fig. S4 in SM.

Figure 5.

Photoluminescence spectroscopy is a valuable tool for obtaining electronic, optical and photoelectric properties of luminescent materials. Photoluminescence spectra are correlated with the particle size, defects and impurities present in the materials. As reported in literature [7], it is believed that the luminescent centers formed from Zr^{4+} ions in an asymmetric site surrounded by the oxygen ions, defects or impurities are predominate source of zirconia photoluminescence. In Fig. 5 photoluminescence spectra of zirconia samples are presented. Excitation wavelength was 300 nm, which was selected according to optical absorption spectra of the samples (Fig. 3), since energy of 4.13 eV should be enough even for excitation of pure ZrO_2 trough oxygen vacancies. Photoluminescence spectra for all samples are defined with broad peak from about 350 nm to 450 nm, with max at about 400 nm and a shoulder at

370 nm. Pure ZrO_2 also has shoulders/peaks at 460 nm, 495 nm and 525 nm. All of them can be assigned to the ionized oxygen vacancies, major defects in ZrO_2 nanostructures, recombined with ~~of~~ a photo generated hole in the valence band. The emission bands for all samples, pure and Fe-doped, are peaking at 370 and 392 nm; the highest intensity was observed for pure zirconia. Addition of Fe ions in zirconia matrix reduced the number of available photogenerated charges that undergo radiative recombination due to localization/recombination at dopant centers. Also, broad peaks at 460 nm, 495 nm and 525 nm can be seen only in pure ZrO_2; doping obviously inactivated intraband states (V_{OX}) responsible for these transitions [7].

For identification of dopant ions and various defects in zirconia matrix, EPR technique has been used; experimental details are given in SM. Obtained results are presented in Fig. 6.

Figure 6.

Calculation of the g factor (EPR parameter) ~~gave us possibility~~enabled us to identify the type of oxygen defects and dopant positions, using the following equation [34]:

$$g = \frac{h\nu}{\mu_B \, \mathrm{H}} \qquad (5)$$

where H is the magnetic field (T), ν is the frequency (Hz, s^{-1}), μ_B is the Bohr magneton equal to 9.274×10^{-24} J T^{-1} and h is Planck's constant, 6.626×10^{-34} J s.

In Fig. 6, the EPR spectra of zirconia samples are presented. The spectra of doped ZrO_2 have two prominent signals with g = 4.8 and 4.2, which can be ascribed to isolated Fe^{3+} ions in two different symmetries/crystalline phases. Namely, analogous

signals have been measured and assigned to the presence of iron ions in the monoclinic (g = 4.80) and tetragonal (g = 4.27) crystalline symmetries [20]. So, it can be claimed that dopant ions are present in two different types of sites. These results coincide with XRD measurements which showed that monoclinic and tetragonal crystalline phases are mixed in our samples, except in 20-ZrO_2 where almost pure tetragonal phase is observed. The same change can be seen in Fig. 6, the width of signal at g = 4.80 increases and for highest contents of dopant is just a weak shoulder, due to increased content of tetragonal phase. Peak at g = 4.20 is clearly visible for all concentrations of dopant, even in pure ZrO_2 due to the presence of Fe impurities in the precursors used for synthesis. The most intensive, broad signal in all spectra is at g ~ 2; the width of this signal is increasing with increasing iron ions content, most probably because of the presence of both $Fe^{2+}$and Fe^{3+}ions as proposed by Zhou and Kittilstved [35]. This signal can have different origins: it can be assigned to iron ions in interaction / not isolated [20], to Zr^{3+} ions-oxygen vacancies presented as defects in zirconia matrix [20] with signal at g ~ 1.97 already confirmed by UV/Vis absorption and photoluminescence spectroscopy (Figs. 3 and 5), and to the signal of free electron at g = 2.0023. Signals that can be assigned to Zr^{3+} defects were studied in pure ZrO_2 [36]: Zr^{3+} ions in monoclinic ($g_{\perp}$(M) = 1.979; $g_{//}$ (M)=1.964) and tetragonal ($g_{\perp}$(T)=1.979; $g_{//}$ (T) = 1.957) environment [36]. The obtained EPR results suggest that Fe ions were incorporated into the ZrO_2 matrix, in both crystalline phases and on the surface and in the bulk of NPs.

3.3. Photocatalytic properties of zirconia samples

Kinetic curves describing the photocatalytic degradation of TCP using ZrO_2 samples as photocatalysts are presented in Fig. 7a); adsorption curves in the same time frame are presented in Fig. S6 in SM. All samples are photocatalytically active and can be used for degradation of TCP using artificial Solar light. Results were compared with the photocatalytic efficacy of P25 TiO_2 in Figure S8, it was similar to the efficacy of zirconia-based samples. 50% of adsorption/degradation was achieved after 95 min when 10-ZrO_2 was used (after 97 min with TiO_2- Fig. S8), after 100 min with 1-ZrO_2 and 20-ZrO_2, after 115 min with 5-ZrO_2 and after 118 min with pure ZrO_2, the rate constants (K), assuming that photodegradation reaction is of pseudo-first order in the first 90 min, are given in inset. The differences are too small to reasonably ~~make~~ draw a conclusion regarding the best or the worst photocatalyst ~~reasonable~~, but 10-ZrO_2 had the highest rate constant ~~had 10-ZrO_2~~.

Figure 7.

After 4 hours of photocatalytic degradation, TCP residue was between 23 and 10 % of starting concentration, the least efficient being pure zirconia and the most efficient photocatalyst ~~was~~being 20-ZrO_2. The group of doped samples with Fe^{3+} ion concentrations from 1-10 are similar and degraded after 4 hours of photodegradation reactions between 77 and 90 % of TCP. The reason for increase of photocatalytic efficacy ~~can~~ could be more intensive absorption of the visible part of the applied light spectrum (Vitalux lamp) by the composites with higher concentration of the Fe^{3+} ions and oxygen vacancies (Fig.3). ~~Also~~In addition, the hematite part of the nanocomposite

can be active in photodegradation of TCP as mentioned in literature by Bandara et. al [30].

Results of TOC (or DOC- dissolved organic carbon, because of the filtering) after 4 hours of irradiation are presented in Fig.7b. This method is excellent for the evaluation of all intermediates together with the parent TCP compound in the reaction mixture. Obviously, the complete mineralization of TCP cannot be followed simply by measuring ~~of~~ its concentration, there are many intermediates formed after degradation of the parent compound. The best material for mineralization of TCP is zirconia doped with the lowest concentration of iron ions. The TCP residue after 4 hours of photocatalytic reaction was about 10%, organic carbon still present in the reaction solution was less than 20%. All other photocatalysts produced much more persistent intermediates, the highest amount was measured for 10-ZrO_2, almost 73% which is about 5 times more than TCP residue. The same ratio was found for 20-ZrO_2, 5-ZrO_2 had 3 times more TOC present compared to TCP residue. Pure ZrO_2 had also good ratio between TCP residue and TOC, less than 2. This technique showed hidden advantages of Fe- doping of zirconia matrix.

The photocatalytic process starts with the absorption of photons with appropriate energy, by the photocatalyst and the excitation of electrons from the valence band to the conduction band and generation of electron/hole pairs [19]. Fe^{3+} ions in matrix can react with photogenerated holes and form Fe^{4+}, in this way holes can migrate (by "jumping" from Fe^{4+} to Fe^{3+}) to the surface and react with adsorbed hydroxyl ions to produce hydroxyl radicals [19]. Also, dopant ferric ions (Fe^{3+}) at the surface of doped zirconia particles can react with adsorbed water and form an "aqua complex" which can, after excitation with UV photons, form Fe^{2+} ions and hydroxyl radicals [19]. Ferrous ions at

the surface of zirconia particles can get oxidized to ferric by electron-transfer to molecular oxygen that is adsorbed on the surface of ZrO_2. Simultaneously, Fe^{3+} ions can be reduced by trapping photogenerated electrons. As stated by crystal field theory, Fe^{4+} and Fe^{2+} ions are unstable compared to Fe^{3+} ions which have half-filled 3d electronic configuration ($3d^5$) [19]. Consequently, by electron transfer of trapped charges from unstable ions, Fe^{3+} ions can be regenerated and can participate again in photocatalytic reactions [19]. At higher dopant concentrations (10 and 20 %), the space between trapping sites/dopant ions decreases significantly and Fe^{3+} ions can act as recombination centers of photogenerated charges; this process is not beneficial for photocatalytic activity [19]. All described charge transfer processes are presented in the scheme in Fig. 8 for two cases: when NPs are doped with low Fe^{3+} concentration (Fig. 8a, 1-ZrO_2) and nanocomposite (Fig. 8b, 20-ZrO_2). Possible excitations are presented with full arrow lines; transitions which are highly improbable when Solar light is used are presented with dashed arrows (Fig.8b). Valence and conduction band potentials of ZrO_2 were calculated using empirical formulas (6), from the electronegativity and band gap energy of zirconia [37]:

$$E_{VB} = \chi - E_0 + 0.5E_g \quad \text{and} \quad E_{CB} = E_{VB} - E_g \quad (6)$$

χ is the electronegativity of the semiconductor, which is the geometric mean of the electronegativity of the constituent atoms, E_0 is the energy of free electrons on the hydrogen scale (about 4.5 eV), E_g is estimated band gap energy of zirconia from Tauc's plots. According to this equation, the conduction band potential of pure zirconia is at -0.84 eV and the valence band potential is at +3.66 eV. These potentials are presented in Figure 8a together with position of potentials of different defects: V_{ox} and levels induced by doping process $Fe^{3+/4+}$ and $Fe^{3+/2+}$, also potentials of formation of $O_2^{\bullet-}$ from

adsorbed O_2 and $OH^{\bullet}$ from adsorbed OH^- are correlated to predict the way photodegradation process can proceed. These radical species had a major role in the photocatalytic degradation of TCP as was revealed in the degradation experiments with radical scavengers, Figure S7. Tert-Butyl alcohol and p-Benzoquinone were used as scavengers for $OH^{\bullet}$ and $O_2^{\bullet-}$ radicals, respectively. Photocatalytic activity of 1-ZrO_2, 5-ZrO_2 and 20-ZrO_2 decreased significantly when both radical species were excluded from reaction solution, for pure zirconia the major radical was $O_2^{\bullet-}$ radical as mentioned before [13].

Figure 8.

In samples 10- and 20- ZrO_2, the charge carriers may react with dopant ions more than once on their way to the nanoparticle's surface, so their mobility decreases while the probability for the recombination process before they can reach the surface increases, resulting in stagnation of photocatalytic activity [19]. Furthermore, higher surface ~~present~~ presence of metal ions in these samples, as well as hematite phase, may alter the photocatalytic efficiency of the composite semiconductor particles (ZrO_2/Fe_2O_3) due to the decreased free zirconia surface for pollutant adsorption. This leads to differences in surface hydroxyl-ions concentration on ZrO_2 part of NPs with varying Fe-dopant concentration, as already mentioned in discussion of obtained photocatalytic efficacies, which don't follow increase in dopant loadings in an expected/linear way. So, to summarize, the doping of zirconia with Fe^{3+} ions ~~were~~ was beneficial for photocatalytic degradation of TCP; the best result regarding mineralization of TCP was achieved with 1-ZrO_2. The worst photocatalytic efficacy was obtained when 5- ZrO_2 was used as photocatalyst; the reason was probably the partial

formation of zirconium ferrite, leaving much ~~less~~ fewer Fe^{3+} ions for developing defect intraband states responsible for improving photocatalytic efficacy.

Conclusions

The Fe^{3+} doping of ZrO_2 nanoparticles using colloidal chemistry/solvothermal method was successful; a series of zirconia nanopowders with different Fe^{3+} loadings were obtained. The presence of iron ions was proved using EPR and ICP measurements. EPR technique also showed that dopant ions were distributed in both crystalline phases of the zirconia matrix. The incorporation of Fe^{3+} ions induced changes in crystalline phase of the zirconia matrix, from mixed monoclinic/ tetragonal phase to almost pure tetragonal phase (95 %) for the highest doping concentration. Doping didn't change the particle sizes of obtained nanoparticles; they were about 10-15 nm. The particle sizes, ~~were;~~ obviously, depended mostly on applied synthesis procedure and subsequent annealing. Specific surface area of nanopowders was from 50-80 m^2g^{-1}, relatively small, and increasing with increasing dopant concentration. Doping induced the stabilization of the presence of isolated nanoparticles. Optical absorption and luminescence measurements revealed the presence of a great number of intraband defect sites (oxygen vacancies, Fe^{3+}/Fe^{2+} and Fe^{3+}/Fe^{4+} levels). Also, effective band gap of doped nanopowders decreased from 4.5eV for pure zirconia to 2.1 eV for 10 and 20-ZrO_2. Doping of zirconia with Fe^{3+} ions proved to be an excellent way to improve its applicability as a photocatalyst for degradation and mineralization of phenolic pollutants. Special ~~care~~ attention should be paid to the concentration of the dopant – about 1 a.% of nominal concentration proved to be the best according to this study. The

nominal Fe^{3+} dopant concentrations ≥ 10% in zirconia matrix have no beneficial effects to photocatalytic efficacy.

Conflict of Interest

All authors declare that there is no competing interest.

Ackowledgments

The authors are grateful to Dr Miodrag Mitrić, University of Belgrade, Vinča Institute of Nuclear Sciences, Belgrade, Serbia, for XRD measurements and to Dr Vladimir B. Pavlović, University of Belgrade, Institute of Technical Sciences of SASA, Belgrade, Serbia, for TEM measurements. The financial support for this work was provided by the Ministry of Education, Science and Technological Development of Republic of Serbia [OI 172056 and III 45020].

Supplementary Material: Details regarding samples characterization, photodegradation method and analytical techniques; Figure S1: XRD patterns of as prepared and annealed pure and doped zirconia nanopowders; Figure S2: Pore size distributions patterns of ZrO_2 samples; Figure S3: N_2 adsorption/desorption isotherms of ZrO_2 samples; Figure S4: Urbach energy plots for pure (a) and doped (b-e) ZrO_2; Figure S5 The Commission International De I-Eclairage (CIE) 1931 chromaticity coordinates of nanomaterials; Figure S6 Adsorption of TCP on applied photocatalysts, marked in figure; Figure S7 The influence of added radical scavengers on remaining TCP concentration in reaction mixture, after 240 min of photocatalytic degradation. TB-tert-butyl alcohol ($OH^{\bullet}$ radical scavenger), BQ-p-benzo quinone ($O_2^{\bullet-}$ radical

scavenger). Figure S8 Kinetic curves of photocatalytic degradation of TCP using zirconia samples and P25 TiO_2 as catalysts.

References:

[1] T. Yamaguchi, Application of ZrO_2 as a catalyst and a catalyst support, Catal. Today 20 (1994) 199-218.

[2] P.A. Deshpande, S. Polisetti, G. Madras, Rapid synthesis of ultrahigh adsorption capacity zirconia by a solution combustion technique, Langmuir 27 **(**2011) 3578-3587.

[3] T. Liu, X. Zhang, L. Yuan, Y. Jingkun, A review of high-temperature electrochemical sensors based on stabilized zirconia, Solid State Ionics, 283 **(**2015) 91–102.

[4] J.H. Shim, C-C Chao, H. Huang, F.B. Prinz, Atomic layer deposition of yttria-stabilized zirconia for solid oxide fuel cells, Chem Mater, 19 **(**2007) 3850-3854.

[5] S. Chang, R. Doong, The effect of chemical states of dopants on the microstructures and band gaps of metal-doped ZrO_2 thin films at different temperatures, J. Phys. Chem. B, 108 (2004) 18098 - 18103.

[6] S.N. Basahel, T.T. Ali, M. Mokhtar, K. Narasimharao, Influence of crystal structure of nanosized ZrO_2 on photocatalytic degradation of methyl orange, Nanoscale Res. Lett. 10 (2015) 73.

[7] S. Kumar, A.K. Ojha, Oxygen vacancy induced photoluminescence properties and enhanced photocatalytic activity of ferromagnetic ZrO_2 nanostructures on methylene blue dye under ultra-violet radiation, J. Alloy Compd. 644 (2015) 654–662.

[8] A.G. Alalm, A. Tawfik, S. Ookawara, Solar photocatalytic degradation of phenol by TiO_2/AC prepared by temperature impregnation method, Desalin. Water Treat. (2014) 1-10.

[9] J. Schneider, M. Matsuoka, M. Takeuchi, J. Zhang, Y. Horiuchi, M. Anpo, D. Bahnemann, Understanding TiO_2 photocatalysis: mechanisms and materials, Chem. Rev. 114 (2014) 9919−9986.

[10] A.V. Emeline, G.N. Kuzmin, D. Purevdorj, V.K. Ryabchuk, N. Serpone, Spectral dependencies of the quantum yield of photochemical processes on the surface of wide band gap solids. 3. Gas/solid systems, J. Phys. Chem. B, 104 (2000) 2989-2999.

[11] Z. Shu, X. Jiao, D. Chen, Synthesis and photocatalytic properties of flower-like zirconia nanostructures, CrystEngComm, 14 (2012) 1122 - 1127.

[12] C. Karunakaran, R. Dhanalakshmi, P. Gomathisankar, Phenol-photodegradation on ZrO_2. Enhancement by semiconductors, Spectrochim. Acta A, 92 (2012) 201– 206.

[13] M.V. Carević, N.D. Abazović, T.B. Novaković, V.B. Pavlović, M.I. Čomor, Zirconium dioxide nanopowders with incorporated Si^{4+} ions as efficient photocatalyst for degradation of trichlorophenol using simulated solar light, Appl. Catal. B- Environ., 195 (2016) 112–120.

[14] M.V. Carević, N.D. Abazović, T.D. Savić, T.B. Novaković, M.D. Mojović, M.I. Čomor, Structural, optical and photodegradation properties of pure and Fe-doped titania nanoparticles probed using simulated Solar light, Ceramics International, 42 (2016) 1521-1529.

[15] M.V. Carević, N.D. Abazović, T.D. Savić, T.B. Novaković, D.J. Pjević, M.I. Čomor, Binary oxide ceramics for enhanced phenols degradation under simulated Solar light, J. Am. Ceram. Soc., 101 (2018) 1420-1431.

[16] M.V. Carević, N.D. Abazović, M.N. Mitrić, G. Ćirić-Marjanović, M.D. Mojović, S.P. Ahrenkiel, M.I. Čomor, Properties of Zirconia/Polyaniline hybrid nanocomposites and their application as photocatalysts for degradation of model pollutants, Mater. Chem. Phys., 205 (2018) 130 – 137.

[17] T. López, M. Alvarez, F. Tzompantzi, M. Picquart, Photocatalytic degradation of 2,4-dichlorophenoxiacetic acid and 2,4,6-trichlorophenol with ZrO_2 and Mn/ZrO_2 sol-gel materials, J. Sol-Gel Sci. Techn., 37 (2006) 207–211.

[18] C. Gionco, M.C. Paganini, M. Chiesa, S. Maurelli, S. Livraghi, E. Giamello, Cerium doped zirconium dioxide as a potential new photocatalytic material. The role of the preparation method on the properties of the material, Appl. Catal. A- Gen., 504 (2015) 338–343.

[19] K. Gurushantha, K.S. Anantharaju, H. Nagabhushana, S.C. Sharma, Y.S. Vidya, C.S Shivakumara, H.P. Nagaswarupa, S.C. Prashanta, M.R. Anilkumar, Facile green fabrication of iron-doped cubic ZrO_2 nanoparticles by *Phyllanthus acidus*: Structural, photocatalytic and photoluminescent properties. J. Mol. Catal. A – Chem., 397 (2015) 36‑47.

[20] F. Wyrwalski, J.F. Lamonier, S. Siffert, E.A. Zhilinskaya, L. Gengembre, A. Aboukaïs, Bulk and surface structures of iron doped zirconium oxide systems: Influence of preparation method, J. Mater. Sci., 40 (2005) 933-942.

[21] S. Kumar, S. Bhunia, J. Singh, A.K. Ojha, Absence of room temperature ferromagnetism in Fe stabilized ZrO_2 nanostructures and effect of Fe doping on its structural, optical and luminescence properties, J. Alloy Compd., 649 (2015) 348-356.

[22] J.A. Navío, M.C. Hidalgo, G. Colón, S.G. Botta, M.I. Litter, Preparation and physicochemical properties of ZrO_2 and Fe/ZrO_2 prepared by a sol-gel technique, Langmuir, 17 (2001) 202-210.

[23] J. Z. Jiang, F.W. Poulsen, S. Mørup, Structure and thermal stability of nanostructured iron-doped zirconia prepared by high-energy ball milling, J. Mater. Res., 14 (1999) 1343 – 1352.

[24] Q. Chen, W. Yang, J. Zhu, L. Fu, D. Li, L. Zhou, In situ fluorine doped ZrO_{2-x} nanotubes for efficient visible light photocatalytic activity, J. Mat. Sci: Mat. Electr. https://doi.org/10.1007/s10854-018-0339-8

[25] Y. Wang, Y. Zhang, H. Lu, Y. Chen, Z. Liu, S. Su, Y. Xue, J. Yao, H. Zeng, Novel N-doped ZrO_2 with enhanced visible-light photocatalytic activity for hydrogen production and degradation of organic dyes, RCS Adv., 8 (2018) 6752-6758.

[26] L. Li, L. Wang, W. Zhang, X. Zhang, X. Chen, X. Dong, Urchin-like CdS/ZrO_2 nanocomposite prepared by microwave-assisted hydrothermal combined with ion-exchange and its multimode photocatalytic activity, J. Nanopart. Res., 16 (2014) 2753.

[27] R. S. Das, S.K. Warkhade, A. Kumar, A.V. Wankhade, Graphene oxide ‐based zirconium oxide nanocomposite for enhanced visible light ‐driven

photocatalytic activity, Res. Chem. Intermediat. https://doi.org/10.1007/s11164-018-3699-z

[28] Ch.V. Reddy, B. Babu, I.N. Reddy, J. Shim, Synthesis and characterization of pure tetragonal ZrO_2 nanoparticles with enhanced photocatalytic activity, Ceram. Int. 44 (2018) 6940-6948.

[29] S. Chang, R. Doong, Chemical-composition-dependent metastability of tetragonal ZrO_2 in sol-gel-derived films under different calcination conditions, Chem. Mater., 17 (2005) 4837-4844.

[30] J. Bandara, J.A. Mielczarski, A. Lopez, J. Kiwi, 2. Sensitized degradation of chlorophenols on iron oxides induced by visible light. Comparison with titanium oxide, Appl. Catal. B – Environ., 34 (2001) 321 – 333.

[31] H. Khan, I.K. Swati, Fe^{3+}-doped anatase TiO_2 with d−d transition, oxygen vacancies and Ti^{3+} centers: synthesis, characterization, UV−vis photocatalytic and mechanistic studies, Ind. Eng. Chem. Res., 55 (2016) 6619−6633.

[32] S.A. Shahid, A. Nafady, I. Ullah, Y.H. Taufiq-Yap, I. Shakir, F. Anwar, U. Rashid, Characterization of newly synthesized $ZrFe_2O_5$ nanomaterial and investigations of its tremendous photocatalytic properties under visible light irradiation, J Nanomater. (2013) 517643.

[33] T.V. Perevalov, A.V. Shaposhnikov, K.A. Nasyrov, D.V. Gritsenko, V.A. Gritsenko, V.M. Tapilin, Electronic Structure of ZrO_2 and HfO_2, in: *Defects in High-k Gate Dielectric Stacks*, Evgeni G. (Eds.), Springer, Dordrecht, 2006: 423 - 434.

[34] S.K.S. Patel, S. Kurian, N.S. Gajbhiye, Room-temperature ferromagnetism of Fe-doped TiO_2 nanoparticles driven by oxygen vacancy, Mat. Res. Bull., 48 (2013) 655‑660.

[35] D. Zhou, K.R. Kittilstved, Control over Fe^{3+} speciation in colloidal ZnO nanocrystals, J. Mater. Chem. C 3 (2015) 4352 – 4358.

[36] N. Sergent, J.-F. Lamonier, A. Aboukaïs, Electron paramagnetic resonance in combination with the thermal analysis, X-ray diffraction, and raman spectroscopy to follow the structural properties of $Zr_xCe_{1-x}O_2$ solid systems and precursors, Chem. Mater., 12 (2000) 3830-3835.

[37] Y. Xu, M.A.A. Schoonen, The absolute energy positions of conduction and valence bands of selected semiconducting minerals, Am. Mineral., 85 (2000) 543–556.

Figure Captions

Figure 1. XRD patterns of zirconia samples. Peaks are assigned according to monoclinic and tetragonal zirconia crystalline phases; the peak assigned to hematite is marked with a star.

Figure 2. TEM images of pure and doped samples: a) ZrO_2, b) 1-ZrO_2, c) 5-ZrO_2, d) 10-ZrO_2, e) 20-ZrO_2.

Figure 3. a) UV/Vis Reflectance and b) absorption spectra of pure and Fe^{3+}-doped zirconia NPs.

Figure 4. Tauc's plots of pure and doped ZrO_2 samples.

Figure 5. Photoluminescence of the zirconia samples excited with λ_{exc} = 300 nm. The Commission International De I-Eclairage (CIE) 1931 chromaticity coordinates for ZrO_2 and Fe^{3+} doped zirconia NPs versus Fe^{3+} concentration is given in Fig. S5 in SM.

Figure 6. EPR spectra of pure and doped zirconia samples.

Figure 7. a) Kinetic curves of photocatalytic degradation of TCP using zirconia samples as catalysts and rate constants in the first 90 min; adsorption curves are presented in SM, Fig. S6. b) TOC and TCP residues after 240 min of photocatalytic degradation.

Figure 8. Proposed charge transfer processes in two cases: a) low dopant concentration and b) with formation of hematite/zirconia nanocomposite (20-ZrO_2).

Table Captions

Table 1. Share (in percentage) of tetragonal and monoclinic crystalline phases in zirconia samples, calculated using equation (2) and crystalline domains of zirconia powders calculated from XRD data.

Table 2 Textural properties of zirconia samples.

Table 3 Band gap and Urbach energies of pure and doped ZrO_2 samples.

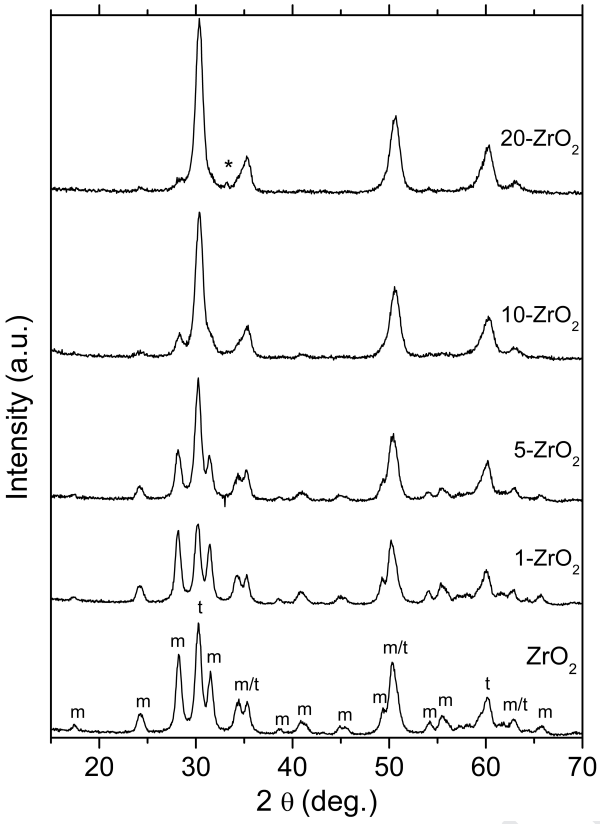

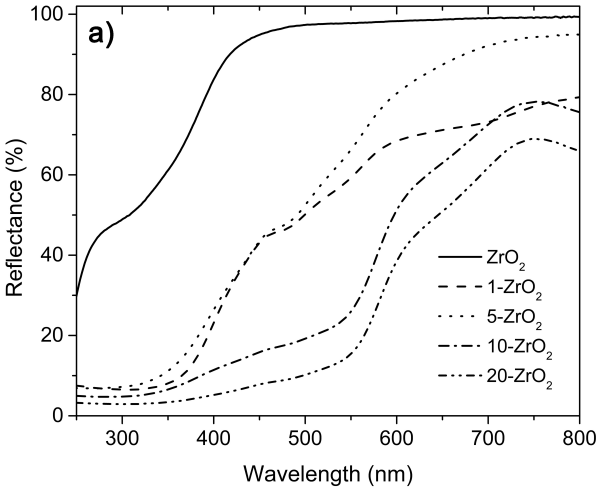

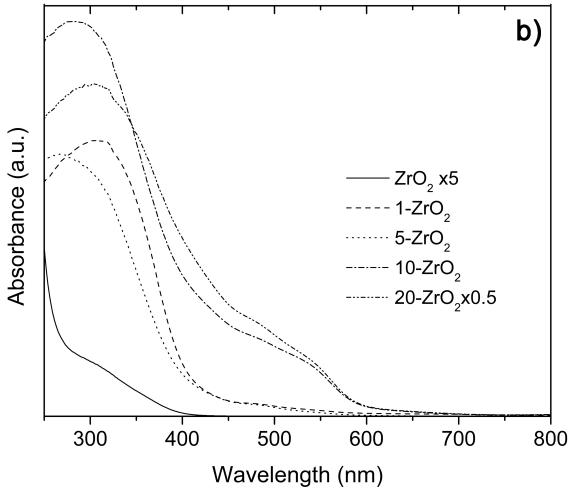

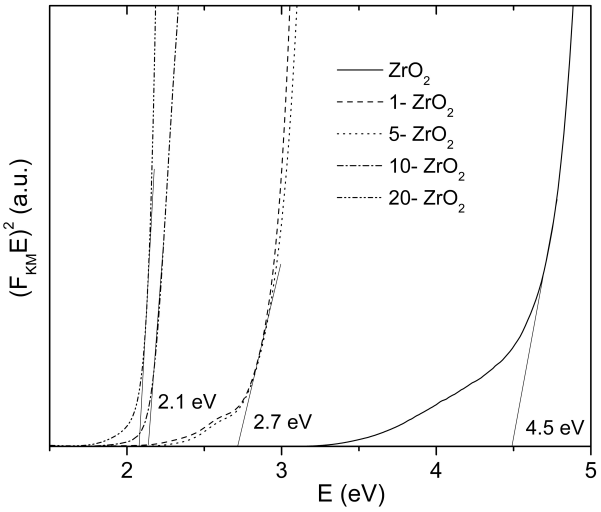

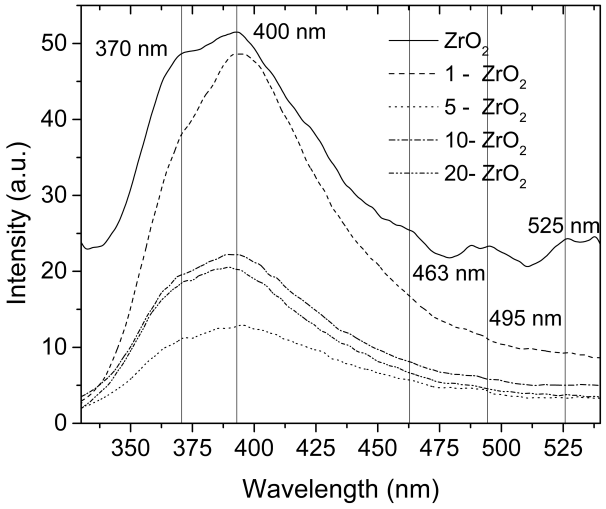

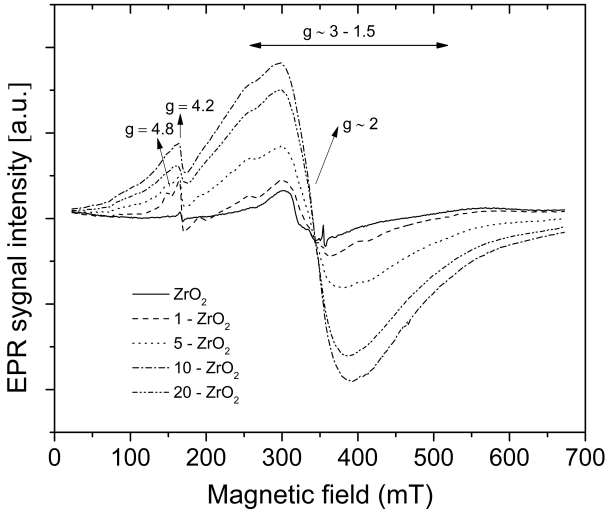

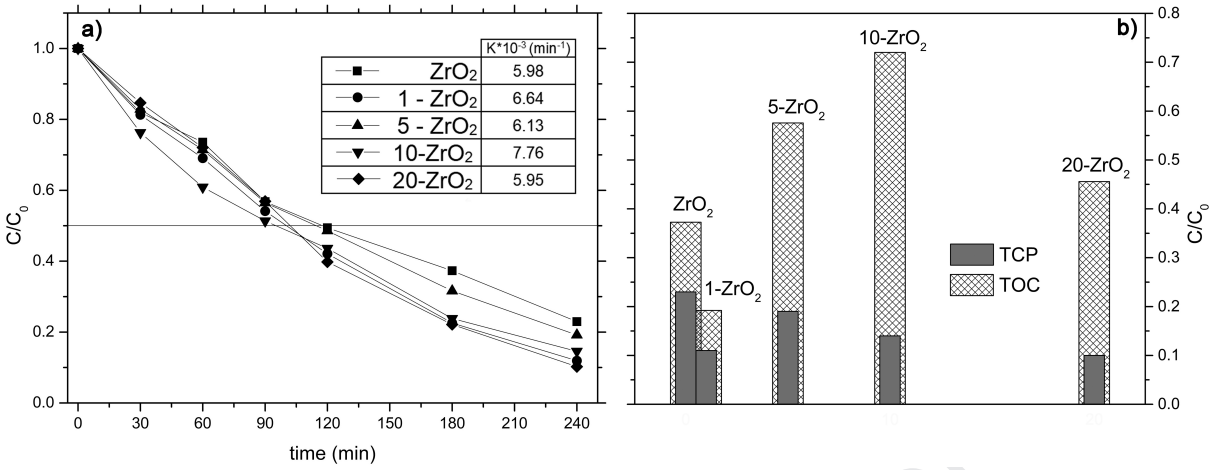

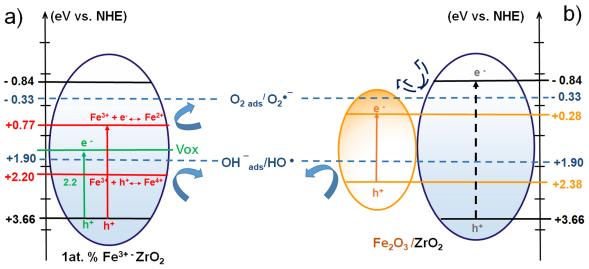

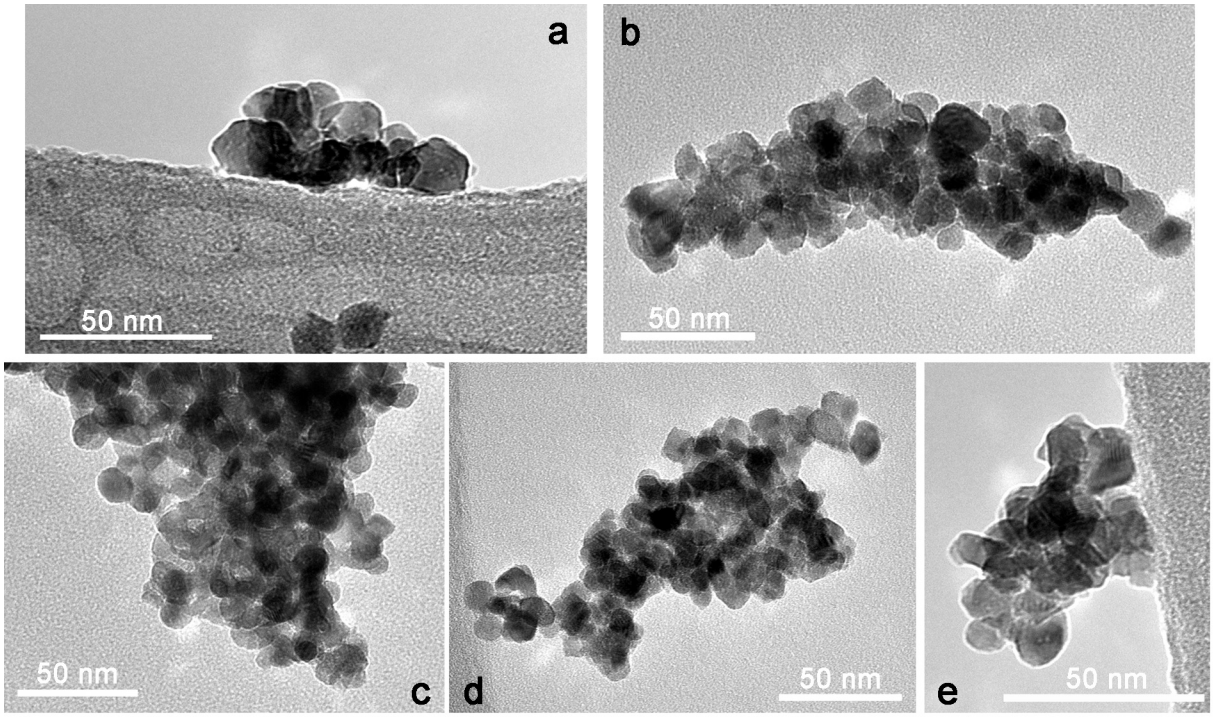

Declaration of interests

☒ The authors declare that they have no known competing financial interests or personal relationships that could have appeared to influence the work reported in this paper.

☐The authors declare the following financial interests/personal relationships which may be considered as potential competing interests: